Hindawi
International Journal of Energy Research
Volume 2024, Article ID 7961519, 13 pages
https://doi.org/10.1155/2024/7961519

Research Article

Effects of Gas-Diffusion Layers and Water Management on the Carbon Corrosion of a Catalyst Layer in Proton-Exchange Membrane Fuel Cells

Sumin Lee,[1,2] Changki Kim,[1] Eunjik Lee,[1,3] Yoon-Young Choi,[1] Sung Yong Jung,[4] Young-Jun Sohn,[1,3] and Hwanyeong Oh[1,3]

[1]*Fuel Cell Laboratory, Korea Institute of Energy Research, 152 Gajeong-ro, Yuseong-gu, Daejeon 34129, Republic of Korea*
[2]*Department of Mechanical Convergence Engineering, Hanyang University, 222 Wangsimni-ro, Seongdong-gu, Seoul 04763, Republic of Korea*
[3]*Hydrogen Energy Engineering, University of Science and Technology, 217 Gajeong-ro, Yuseong-gu, Daejeon 34113, Republic of Korea*
[4]*Department of Mechanical Engineering, Chosun University, 309 Pilmun-Daero, Dong-gu, Gwangju 61452, Republic of Korea*

Correspondence should be addressed to Hwanyeong Oh; hyoh@kier.re.kr

Received 8 November 2023; Revised 9 February 2024; Accepted 2 April 2024; Published 30 April 2024

Academic Editor: Samuel Lalthazuala Rokhum

Carbon corrosion in a catalyst layer (CL) deteriorates the performance and durability of proton-exchange membrane fuel cells (PEMFCs), which are closely related to water management within these cells. This study investigates the characteristics of water behavior of two gas diffusion layers (GDLs) and compares their influence on degrees of degradation in the CL. First, the properties of the GDLs, including their thickness, pore size distribution, gas permeability, electrical resistance, contact angle, and polytetrafluoroethylene (PTFE) content, are evaluated. The dynamic behavior of liquid water is observed using a visualization cell and synchrotron X-ray imaging. Second, a modified accelerated stress test (AST), which includes a water generation reaction within the catalyst support protocol of the US Department of Energy (DOE), is performed. For assessing the degradation, we utilize polarization curves, electrochemical impedance spectroscopy, cyclic voltammetry, scanning electron microscopy, and field emission transmission electron microscopy. The results reveal that, even though GDL B contains a higher hydrophobic content than GDL A, it exhibits lower water discharge, indicating a reduced performance at high relative humidity (RH) levels. This is attributed to a low capillary pressure gradient, which is influenced not only by PTFE but also by the overall pore structure (i.e., porosity and pore size). Consequently, a high capillary pressure gradient can enhance water discharge and thereby mitigate carbon corrosion and Pt agglomeration in the CL. In addition, the application of the modified AST induces carbon corrosion with fewer cycles than that achieved using the DOE carbon support protocol.

1. Introduction

Proton-exchange membrane fuel cells (PEMFCs) are energy conversion devices that directly convert the chemical energy of a reactant into electric energy [1, 2]. Some important advantages of PEMFCs are their high energy conversion rate, high power density, low emissions, easy scale-up, and fast startup [3–8]. PEMFCs are mainly composed of a bipolar plate, catalyst layer (CL), membrane, and gas diffusion layer (GDL). The GDL is composed of a macroporous substrate and a microporous layer (MPL). The substrate is made of carbon fibers and polytetrafluoroethylene (PTFE), while the MPL is composed of carbon particles and PTFE. PTFE enhances the hydrophobicity of the GDL. The hydrophobic nature of the GDL plays a crucial role in the removal of water [9, 10]. Note that PEMFCs need to be sufficiently humidified to be able to transfer protons through the electrolyte. During the operation of PEMFCs, water is generated as a byproduct of the electrochemical reaction at the cathode. Depending on operating conditions, excess water can

accumulate internally, leading to flooding. As a result, oxygen cannot reach the CL, resulting in performance degradation.

It is essential to ensure the durability of commercial fuel cells, which is affected by various factors. Carbon corrosion is one such critical factor. PEMFCs undergo carbon corrosion during their startup and shutdown, as well as during fuel starvation. A hydrogen/air interface forms under such conditions, which generates a high electrode potential at the cathode. This phenomenon, known as the "reverse-current mechanism" [11], results in the water electrolysis reaction (WER) (Equation (1)) as well as the carbon oxidation reaction (COR) (Equation (2)) [12, 13].

$$2H_2O \longrightarrow O_2 + 4H^+ + 4e^- (\text{WER}) \quad (1)$$

$$C + 2H_2O \longrightarrow CO_2 + 4H^+ + 4e^- (\text{COR}) \quad (2)$$

As both the CL and GDL are predominantly composed of carbon, they are highly susceptible to carbon corrosion, which causes significant changes in their material properties and structures. These changes can degrade the performance of PEMFCs. Many studies have examined the effects of carbon corrosion. Saha et al. [14] utilized the accelerated stress test (AST) developed by the United States Department of Energy (DOE) to observe the morphological changes caused by carbon corrosion of the cathode CL. They divided these changes into those occurring in the initial and later phases of corrosion. Previous studies have reported a rapid rate of carbon corrosion, a fast reduction in the thickness of the CL, and a quick loss in the electrochemically active surface area (ECSA) during the initial phase of carbon corrosion. A dramatic collapse of the pore structure was observed during the later phase of corrosion. Ha et al. [15] applied 1.45 V to induce carbon corrosion in the GDL and conducted a 96 h test to assess the effects of corrosion. They observed a decrease in the weight and thickness of the GDL after the test. Furthermore, scanning electron microscopy (SEM) analysis revealed that carbon corrosion causes structural damage, which decreases the water removal capability, thereby deteriorating the performance. Yu et al. [16] conducted an accelerated degradation test on the GDL under a constant voltage of 1.25 V to observe its corrosion behavior. The SEM images obtained after the test revealed the presence of numerous holes and cracks in the oxidized MPL of the GDL. These holes and cracks also explain the PTFE loss accompanied by carbon oxidation, which resulted in a loss of hydrophobicity and subsequent degradation in performance. Xu et al. [17] conducted an AST under a constant potential of 1.42 V for 48 h. A performance evaluation of both aged and pristine GDLs after the AST revealed increased high-frequency resistance (HFR) and increased mass transfer resistance in the high current density region. They attributed this phenomenon to excess water that blocks oxygen transfer. Furthermore, they noted that carbon corrosion was more significant in the MPL, while the loss of PTFE was more pronounced in the substrate.

Previous studies on the carbon corrosion of GDL focused on inducing the degradation of durability by removing the GDL from the cell, which creates a significantly harsher environment than that observed under real cell conditions. Hence, for a more relevant assessment, studies that performed durability acceleration with an assembled fuel cell should be considered. Zhang et al. [18] conducted an AST for carbon corrosion under cell state conditions and tested the cell performance after separating the aged membrane electrode assembly (MEA) and aged GDL. They reported that the primary performance began to degrade when the aged MEA was combined with a fresh GDL, whereas the minimal performance began to degrade when the fresh MEA was combined with an aged GDL. These findings suggest that CL degradation is the main factor contributing to performance degradation. Sim et al. [19] employed two methods for inducing carbon corrosion. The first method involved simulating hydrogen starvation during both startup and shutdown conditions. The second method involved applying cyclic voltages of 1.0 and 1.5 V to the cathode. Similar to Zhang et al. [18], Sim et al. also compared the performance of a combination of aged MEA and fresh GDL with that of fresh MEA and aged GDL. They found that the carbon corrosion of the MEA has a higher detrimental effect on the PEMFC performance than that of the GDL. Hence, in a carbon corrosion environment, the GDL experiences relatively minimal intrinsic degradation compared to that experienced by the CL.

The carbon corrosion rate of the CL can vary based on how water is managed (Equation (2)) [20–23]. Therefore, it is essential to conduct research on carbon corrosion within the CL, particularly in relation to the GDL, which plays a crucial role in water management. Many studies have primarily focused on the presence or absence of an MPL. Spernjak et al. [24] studied carbon corrosion in a cathode GDL. They reported that the cell with the MPL incorporated in the GDL exhibited a lower reduction in the ECSA than that in the cell without an MPL in the GDL under a 1.3 V holding condition at 80°C and RH 100%. Zuo et al. [25] studied performance degradation in relation to the presence or absence of an MPL. They found that during the aging tests, the MPL protected the CL against carbon corrosion and pore structure damage. Furthermore, the MPL improved water transport, which suppressed the increase in mass transfer losses. As the MPL is currently considered an essential component, it is necessary to examine the relationship between the GDL design, water management, and carbon corrosion using quantitative experimental data, focusing on double-layer GDLs that include the MPL.

This study is aimed at analyzing the difference in the carbon corrosion rate of a CL in two commercial GDLs (including the MPL) exhibiting different properties in the assembled fuel cell. The physical properties of the GDLs, such as pore distribution, gas permeability, and electrical resistance, are measured, and the differences in water behavior of the GDLs are experimentally observed using a visualization cell. In addition to using the US DOE catalyst support protocol [26] for inducing carbon corrosion, this study also employed the AST, which includes a constant current operation, to simulate a corrosion environment that reflects the generation and retention of water under actual

operating conditions. To comprehensively assess the degree of degradation, a systematic analysis is performed by combining the electrochemical characterization of the MEAs with a structural investigation of the CL and GDLs using polarization curves, electrochemical impedance spectroscopy (EIS), cyclic voltammetry (CV), SEM, field emission transmission electron microscopy (FE-TEM), energy dispersive X-ray spectroscopy (EDS), and thermogravimetric analysis (TGA). Finally, the capillary pressure gradients are quantitatively compared to understand the water transport phenomena in GDLs. A concise overview of the research is provided in the Supplementary Materials (Figure S1).

2. Materials and Methods

2.1. Electrochemical Analysis. The AST was conducted using a 25 cm^2 single cell with serpentine flow channels at a fuel cell station (Scitech Korea Inc.). The commercial MEA (GFCC0035, GORE® PRIMEA®) consisted of 0.1 and 0.4 mg_{Pt} cm^{-2} of Pt/C catalysts at the anode and cathode, respectively. All the GDLs (JNTG Co., Korea) composed of a substrate and an MPL were assembled using the aforementioned MEA. Throughout the evaluation, the cell temperature, RH, and back pressure were maintained at 80°C, 100%, and atmospheric pressure, respectively. The electrochemical analysis of the single cells was conducted using a potentiostat (HCP-803, BioLogic Science Instrument, France). The following evaluation method was used: (1) activation: to activate the assembled single cell, an activation process was carried out for 3 h. Hydrogen and air were supplied at 0.4 standard liters per minute (SLPM) to the anode and 2 SLPM to the cathode, respectively. To facilitate the activation, cell voltages of 0.4, 0.6, and 0.8 V were repeatedly applied for 2 min each. (2) Polarization curves and EIS: the polarization curves and EIS were measured at the same flow rates as those for the activation process. The polarization curve was obtained by varying the voltage from the open-circuit voltage to 0.3 V at a scan rate of 10 mV s^{-1}. The impedance measurements were conducted in a frequency range of 10^3 kHz to 0.5 Hz at a current density of 1 A cm^{-2} and an amplitude of 0.03 A cm^{-2}. The x-intercept in the high-frequency region was used to determine the HFR value. (3) CV: hydrogen and nitrogen were supplied to the anode (0.2 SLPM) and cathode (1 SLPM), respectively. The current density corresponding to the applied voltage was measured in the voltage range of 0.05–1.2 V at a scan rate of 50 mV s^{-1}.

2.2. AST Protocol. The AST was performed after evaluating the beginning of life (BOL) performance using the aforementioned method. Figure 1 shows the experimental procedures, including a modified AST protocol based on the DOE catalyst support protocol. The original DOE protocol involved a triangle sweep at a scan rate of 500 mV s^{-1} in the high voltage range (1.0–1.5 V), leading to rapid carbon support corrosion. The proposed AST protocol in this study, based on the original DOE method, applied a constant current density (1 A cm^{-2}) to each cell to induce water generation in the CL. This approach facilitates a faster degradation of the carbon support by producing water within the CL. Next, potential cycling (triangle sweep) between 1.0 and 1.5 V was conducted at a scan rate of 500 mV s^{-1} for 1000 cycles. Durability tests are conducted three times, incorporating CV checks at each end of life (EOL), and a final EOL performance involving both CV and polarization curves.

2.3. Material Properties. The thickness, electrical resistance, and gas permeability of each GDL in a compressed state were measured using CPRL10 (Living Care©, Korea). The pore distribution and structural images of the GDLs were characterized using mercury intrusion porosimetry (MIP) (AutoPore IV 9505, Micromeritics, USA) and SEM (Regulus 8220, Hitachi, Japan), respectively. The PTFE contents were analyzed via the EDS using Ultim Max (Oxford Instruments, UK) and TGA (TGA N-1000, sincoM&T, Korea). The contact angle of the GDL was measured using SmartDrop (Femtobiomed, Korea). Microscopic analysis of the CL was performed using FE-TEM (200 kV, JEOL JEM-F200). The size and distribution of the Pt nanoparticles within the CL were calculated using the average value of 200 particles obtained from the FE-TEM images.

2.4. Synchrotron X-Ray Imaging for Visualizing Liquid Water inside GDL. To compare the transport behavior of liquid water inside the GDL, a synchrotron X-ray imaging technique was employed. As shown in Figures 2(a) and 2(b), a visualization cell was specially designed to simulate the actual liquid water transport from the CL to the cathode channel. A gas diffusion electrode (GDE) was inserted between the water channel and the GDL to uniformly supply water and ensure a capillary pressure gradient similar to that under the actual operating conditions. The sample thickness was set with a compression rate of 10%, which was ensured using a noncompressible sheet gasket. Additionally, the thickness of the gasket is proportionally reduced as the GDL thickness decreases. A single serpentine channel was used to supply water and air. Water is injected into the GDE side channel. Air was supplied to the GDL side channel to simulate the gas flow in the cathode channel. Figure 2(c) shows the inside of the cell. The widths of both the channels and ribs were 0.8 mm, while the heights of the water and air channels were 0.8 and 0.4 mm, respectively. The flow rates for the water and air were determined by considering the production amount and gas flow velocity under the 1.2 A cm^{-2} condition. The corresponding flow rates were 0.015 and 9.284 mL min^{-1} for the water and air, respectively. Water injection was controlled using a syringe pump. The experiments were conducted at the 6C and 9D beamlines of the Pohang Accelerator Laboratory (Pohang, Korea). The beam storage energy was 3 GeV, and the corresponding beam current was 360 mA.

3. Results and Discussion

3.1. GDL Characteristics. This study uses two GDLs to analyze the effect of carbon corrosion in the CL. Table 1 summarizes the physicochemical properties obtained using the equipment described in Section 2.3. The thicknesses were measured using the aforementioned equipment. The

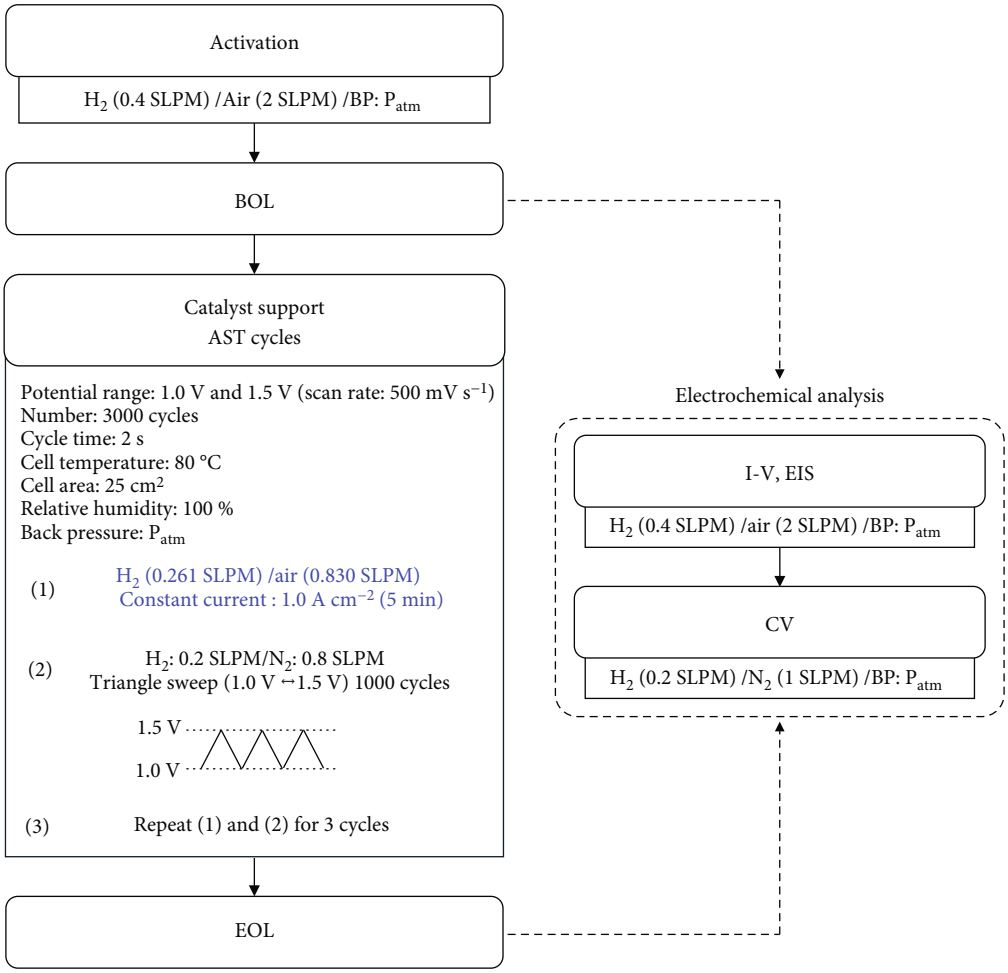

Figure 1: Experimental procedures, including an accelerated carbon corrosion mode modified from the DOE-AST protocol for catalyst support. The modified condition is highlighted in blue.

pore size distribution (PSD) of each GDL was analyzed twice at different locations using the MIP (Figure 3(e)). The differences in surface fluorine content, as determined by EDS analysis, between the two MPLs are less pronounced than the difference in substrates. Additionally, in the MPL surface SEM images of Figures 3(a) and 3(b), a slight difference appears to exist between the MPLs of GDL A and GDL B. Figure 3(e) further demonstrates the minimal difference between the two MPLs. Meanwhile, the GDL B substrate exhibits a relatively higher concentration of fluorine compared to that of GDL A. The SEM image shown in Figure 3(d) confirms the presence of a significant amount of PTFE between the carbon fibers compared to Figure 3(c). However, EDS analysis focuses on the PTFE content present on the surfaces. Consequently, we conducted an additional analysis for the PTFE content using the TGA method, focusing exclusively on the substrate part. Therefore, samples for TGA were prepared by carefully scraping only the substrate. The samples were heated from 23 to 900°C at a rate of 10°C min^{-1} under nitrogen conditions. The initial weight of GDL A was 3.2 mg, while that of GDL B was 3.65 mg. The results are presented in Figure S3. At approximately 550°C, the PTFE contents were 4.73 wt% for GDL A and 11.93 wt% for GDL B. Many studies have indicated that the porosity tends to decrease with an increase in the PTFE contents [27–29]. However, the porosity is affected not only by the PTFE content but also by the carbon fiber structure. We found that even though GDL B contains a higher PTFE content than GDL A, the former exhibits larger pores than the latter. Figure 3(d) and the cross-section of GDL in Figure S2 reveal that GDL B contains coarser fibers than GDL A. This observation is consistent with the PSD results presented in Figure 3(e). Because of these properties, GDL B has an increased electrical resistance and a higher gas permeability. The higher gas permeability suggests that the influence of the fiber structure on the porosity is more significant than that of the PTFE content. In the case of the MPL, both GDL A and GDL B exhibit similar SEM images and PSD analyses.

The water thickness along the X-ray beam path at an arbitrary position can be calculated using the Beer–Lambert law [30]:

$$I = I_0 \exp(-\mu x), \tag{3}$$

where μ is the linear absorption coefficient of water. x is the water thickness. I_0 and I are the incident and transmitted

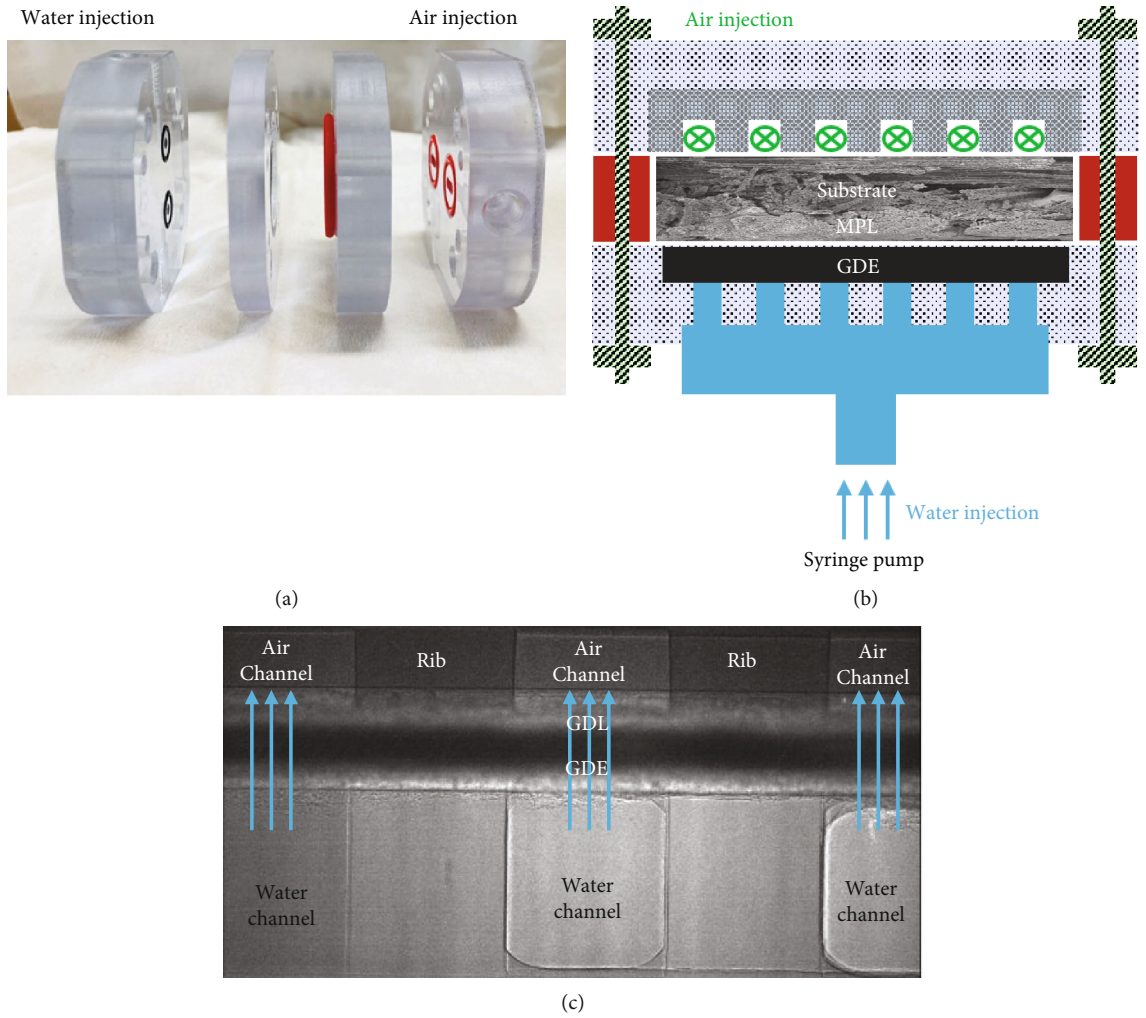

Figure 2: (a) Visualization cell and (b) schematic illustration inside the cell for the synchrotron X-ray imaging of the liquid water behavior through a GDL (c) X-ray image inside the cell.

Table 1: Physicochemical and electrical characterization of GDLs.

Property	Unit	GDL A	GDL B
Thickness*	Mm	192 ± 2.49	158 ± 0.82
Through-plane electrical resistance*	mΩ cm^2	7.57 ± 0.05	8.60 ± 0.19
In-plane electrical resistance* (MD[a]/TD[b])	Ω	0.73 ± 0.02/0.55 ± 0.03	1.04 ± 0.01/0.73 ± 0.01
Through-plane gas permeability**	10^{-12} m^2	0.69 ± 0.03	0.75 ± 0.05
In-plane gas permeability*	10^{-12} m^2	5.33 ± 0.18	6.69 ± 0.26
Contact angle (substrate/MPL)	°	137.50 ± 1.85/148.17 ± 3.73	140.97 ± 3.96/150.16 ± 4.39
Fluorine at MPL surface**	wt%	14.68 ± 0.34	17.62 ± 0.26
Fluorine at substrate surface**	wt%	7.10 ± 0.30	16.97 ± 1.71

*Compressed at 10 kgf cm^{-2}. **Uncompressed. [a]Machine direction. [b]Transverse direction.

intensities of the X-ray beam, respectively. These values are obtained both before and after water injection. Figures 4(a) and 4(b) show temporal variations in the amount of water, converted from the water thickness, passing through the plane direction for GDLs A and B, respectively. The water content of the GDLs increases with time. No sudden increase in water is observed at any location in either GDL in the initial state. Water rapidly increases near the channel because of water stagnation over time. This region, which contains a large amount of water, is thicker in GDL B than

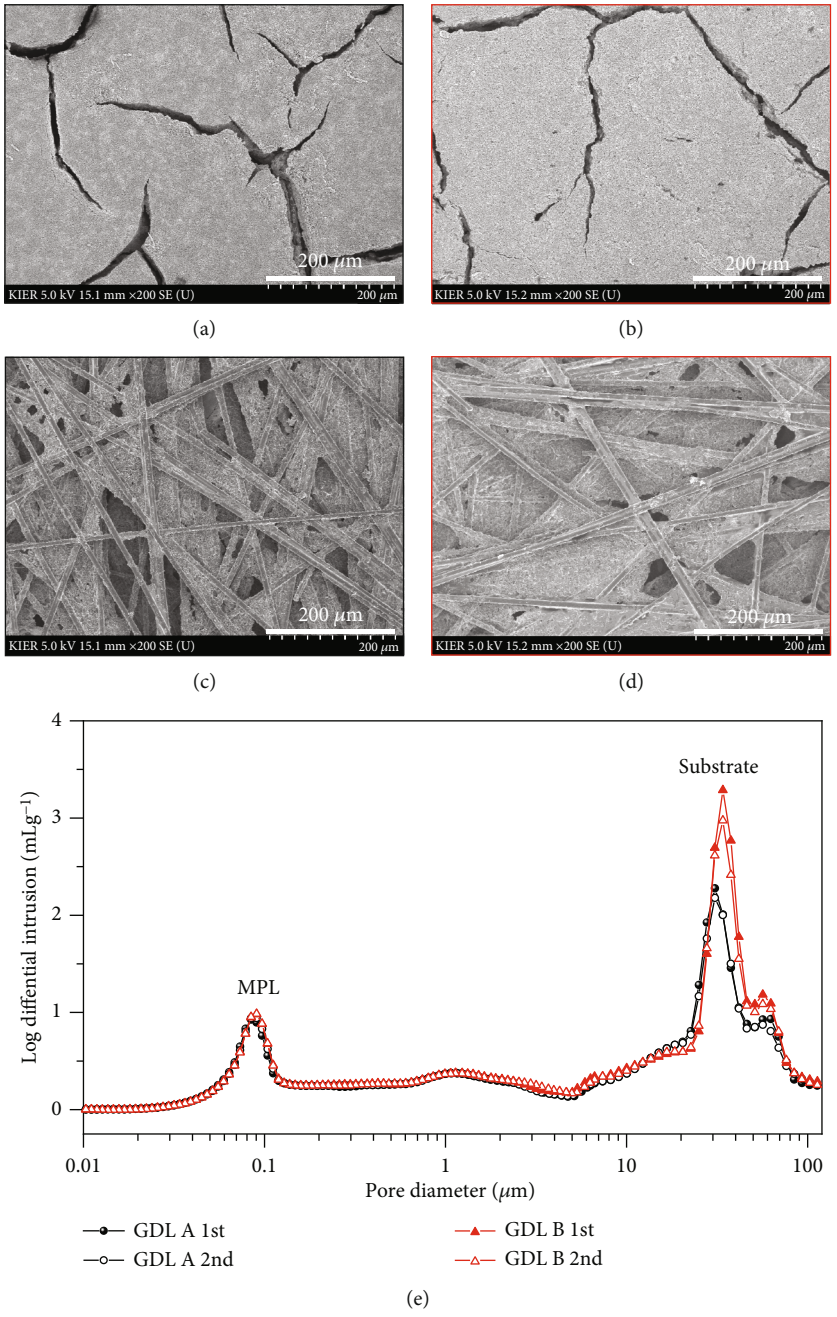

Figure 3: (a–d) SEM images of fresh GDLs (×200 view; top: MPL surface, bottom: substrate surface, left: GDL A, right: GDL B) and (e) pore size distributions of GDLs.

it is in GDL A. The time-varying amounts of liquid water in the entire GDLs are compared in Figure 4(c). The amounts of water in both GDLs are comparable until 460 s when the amount of water rapidly increases. A breakthrough, that is the initial water penetration into the channel from the GDL, occurs at this time. After the breakthrough, the amount of water inside each GDL becomes significantly different. Compared to GDL A, a larger amount of water is observed in GDL B, which is thinner and has more PTFE. More water in GDL B indicates a lower permeability of liquid water.

3.2. Electrochemical Performance. Figure 5 shows various electrochemical performance evaluation results, both before and after the AST. As seen in Figure 5(a), the initial performance (before AST) of single cells with both GDLs shows no significant difference in the low and middle current density regions. However, cells with GDL A exhibit better cell performance than that of the cells with GDL B in the high current density region. The performance of GDL B was consistently lower in all the polarization curves measured every 1000 cycles (Figure S4). The performance difference in the high current density region increased on increasing the

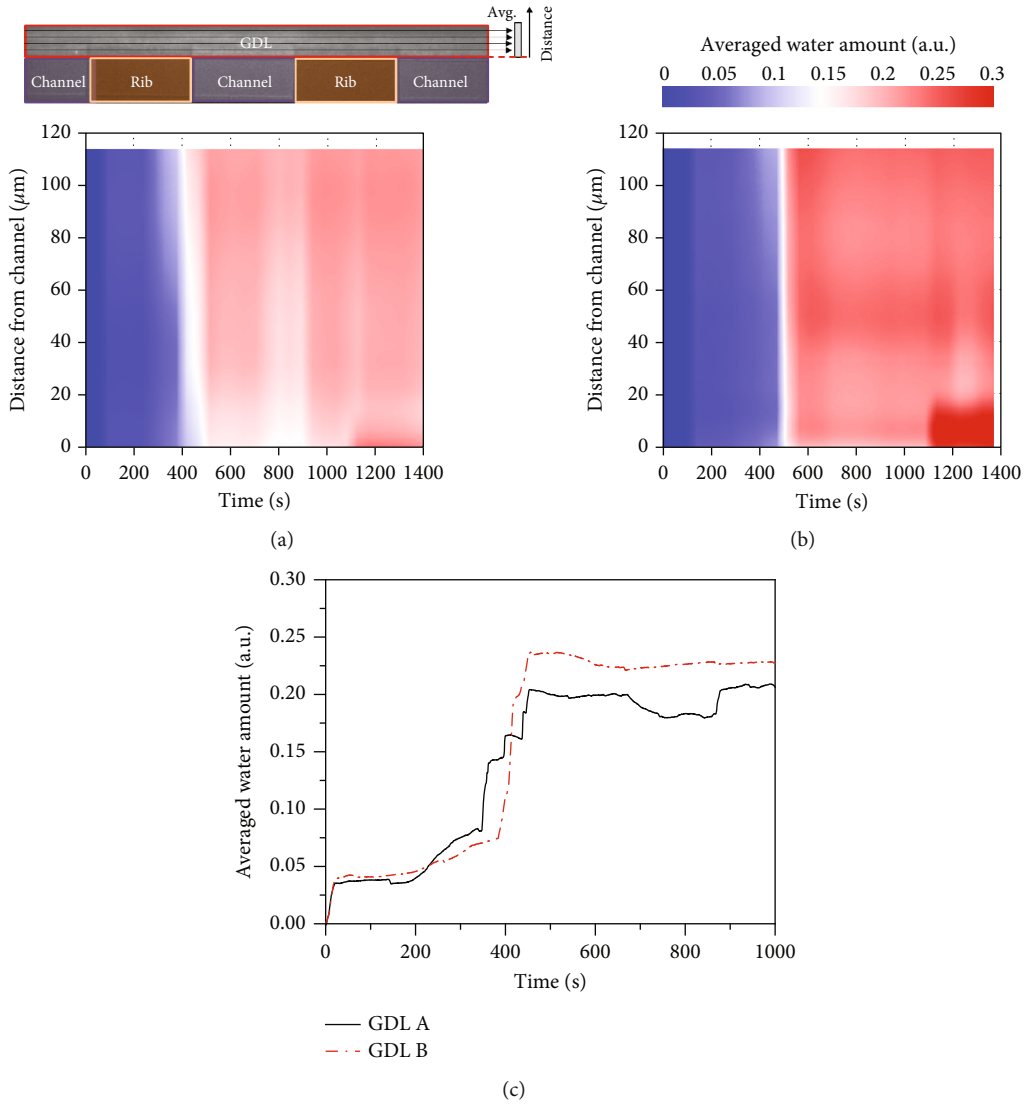

Figure 4: Time-variant amount of liquid water transferred along the through-plane of (a) GDL A, (b) GDL B, and (c) average amount through the plane of each GDL.

number of cycles. This disparity in performance at high current density region can be attributed to the difference in the water management ability of GDLs, which greatly affects the mass transport loss. Furthermore, when the same current density (1.0 A cm^{-2}) was used, the performance of A and B decreased by 26.6% and 42.4%, respectively. Figure 5(b) shows the EIS data for single cells. The EIS is used to analyze the electrochemical behavior of a fuel cell by measuring its impedance response over a range of frequencies. The difference in the HFR values based on the influence of water management can also be seen in the EIS results shown in Figure 5(b). As shown in Figure 4, GDL B exhibits a lower water permeability, making it more susceptible to flooding. The Nyquist plot in Figure 5(b) confirms that the ohmic, charge transfer, and mass transfer resistances increase after the degradation test. The fact that GDL B exhibits high impedance but low HFR supports the possibility of flooding. In addition, compared to GDL A, larger changes in the abovementioned resistances are observed with GDL B. This phenomenon can be attributed to the poorer water management with GDL B, which causes a voltage drop because of flooding in the entire electrode layer. These results indicate that the water management capability of the GDL can accelerate the degradation of the carbon support in the CL and significantly affect the performance decline owing to degradation. Detailed information regarding water transport in the GDL is presented in Section 3.4. Figures 5(c) and 5(d) show the CV data before and after the durability test of the cells containing GDLs A and B, respectively, as well as the change in the ECSA measured every 1000 cycles. As shown in Figure 5(c), the initial ECSA values of both cells are similar because the same catalyst-loaded MEA is used. After the AST, a significant decrease in the ECSA can be observed in both single cells, which is attributed to the degradation of the support material within the CL. In addition, a significant decrease in the ECSA is observed in the GDL B cell, where the degradation of the support material occurs more prominently than it does in the GDL

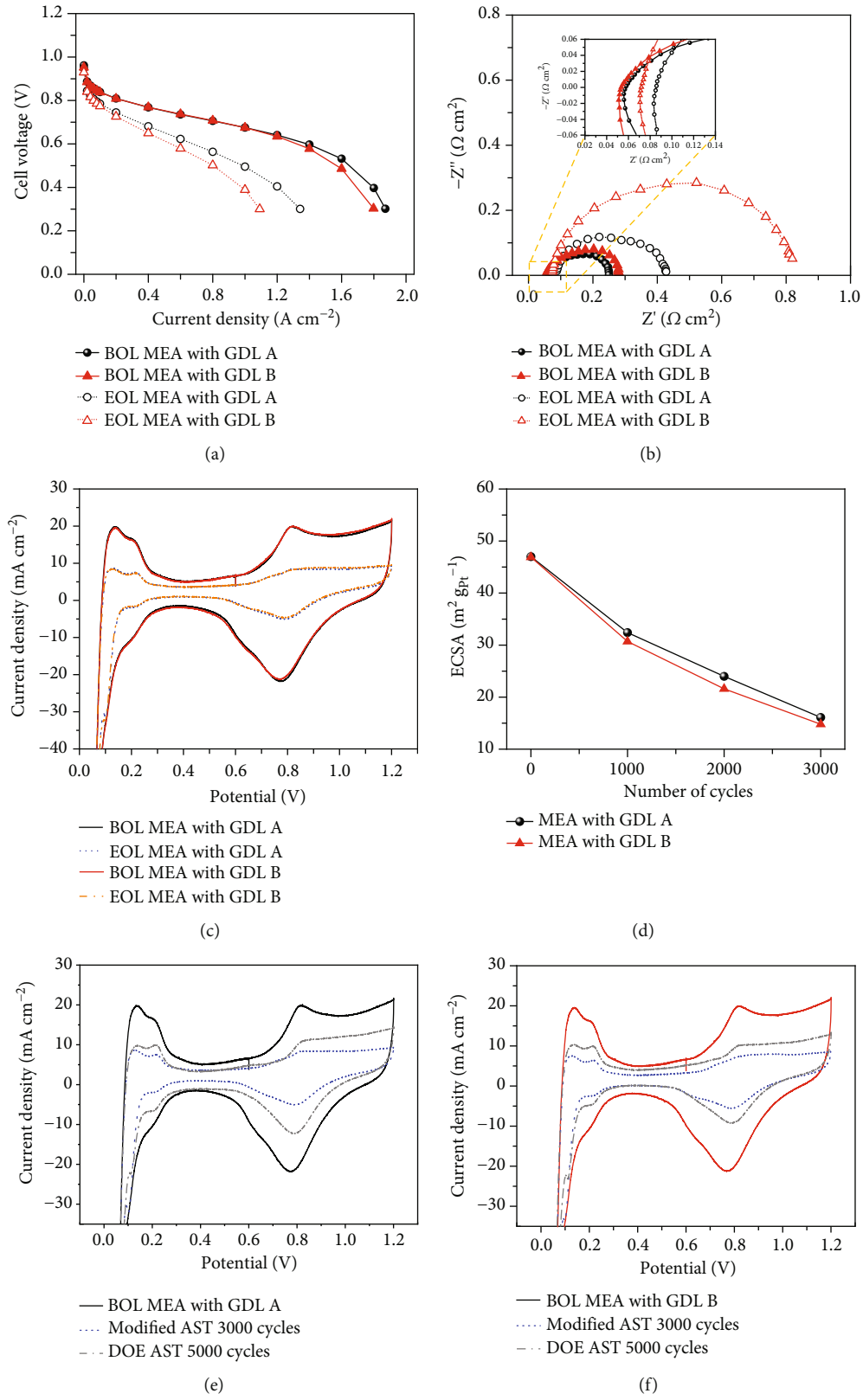

Figure 5: Electrochemical performance of MEA with both GDL A and GDL B before and after 3000 cycles of AST. (a) Polarization curve, (b) galvanostatic EIS at 1.0 A cm^{-2}, (c) CVs, (d) ECSA change of MEA, and comparison of the degradation effect between the modified protocol and DOE AST protocol using CV: (e) MEA with GDL A and (f) MEA with GDL B.

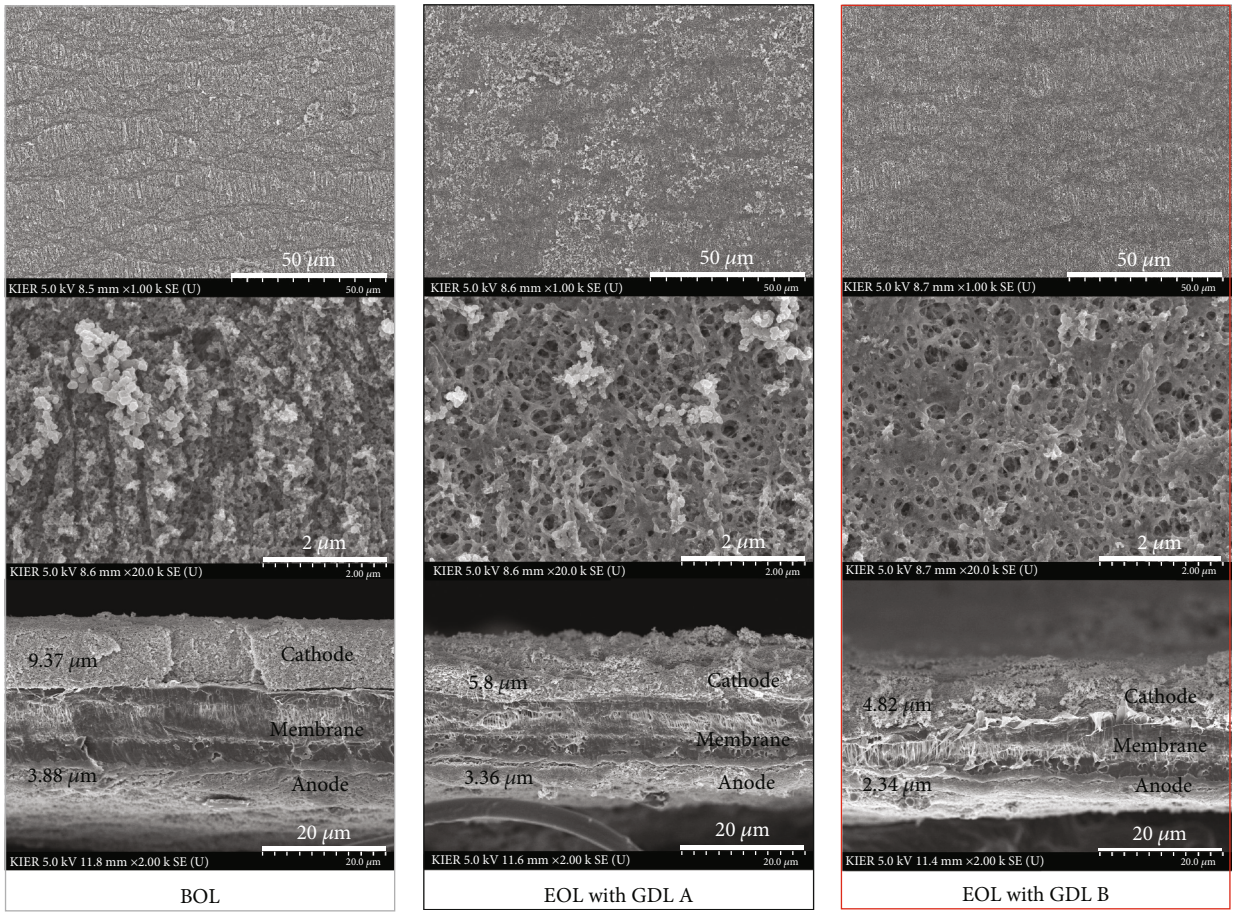

Figure 6: SEM images of the (a) BOL MEA and EOL MEA (b) with GDL A and (c) with GDL B (1st row: cathode surface ×1 k view, 2nd row: cathode surface ×20 k view, 3rd row: cross-section ×2 k view).

A cell (Figure 5(d)). Figures 5(e) and 5(f) compare the CV data of the original DOE protocol with our newly developed AST protocol. The new protocol demonstrates significant changes in the ECSA, even with fewer cycles than that observed in the original DOE protocol. A possible reason for this result is the promotion of water generation within the CL through constant current operation every 1000 cycles. This result suggests that water within the CL has a significant impact on the durability of the support material.

3.3. Change in Material Structure. Figures 6(a)–6(c) show the top and cross-sectional SEM images of the MEA structure. Specifically, Figure 6(a) depicts the structure before AST, while Figures 6(b) and 6(c) illustrate the structure after AST. The cathode surface images shown in the first and second rows in Figures 6(b) and 6(c) demonstrate that the EOL MEA with GDL B exhibits more changes in its surface structure than that with GDL A. This is because GDL B exhibits higher water retention than GDL A, leading to accelerated carbon corrosion in the MEA with the former. The third row shows cross-sectional images of the MEA. The thickness measurements before and after the AST are obtained by using the ImageJ software [31] and by averaging the measurements taken at 10 different locations in the SEM images. The thickness of the MEA with GDL B shows a greater extent of reduction than that observed for the MEA with GDL A. This result is consistent with the observation of a greater reduction in the ECSA, as shown in Figure 5.

Figures 7(a)–7(c) show the FE-TEM images of the Pt/C catalysts in the cathode before and after the AST. In the BOL MEA, approximately 2.88 nm Pt nanoparticles are uniformly distributed on the carbon support. Furthermore, in the EOL MEA with GDLs A and B, the particle sizes of Pt nanoparticles in the CL increase to 4.70 and 4.83 nm, respectively. As shown in Figure 7(g), the particle size is larger and the particle distribution is wider in the MEA with GDL B. This phenomenon is attributed to the carbon corrosion of the support under high voltage conditions during the AST, leading to particle aggregation and Oswald ripening [32]. Additionally, the temperature-colored TEM images in Figures 7(d)–7(f) show that the carbon support changes from orange in the BOL MEA to yellow in the EOL MEA, indicating that the thickness of the carbon support decreases, the pore structure collapses, and the support becomes amorphous after the AST. Moreover, the degradation of the carbon support is more pronounced in the MEA with GDL B than it is in the MEA with

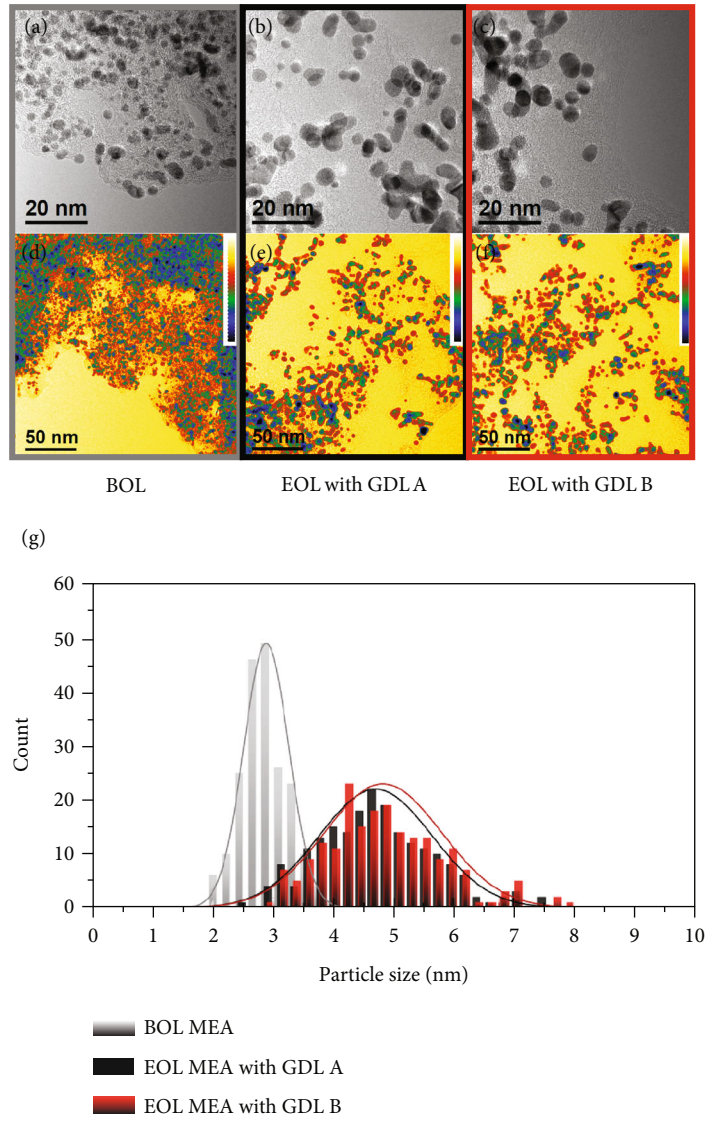

Figure 7: FE-TEM images of Pt/C in the cathode side before and after 3000 cycles of AST. (a, d) BOL MEA, (b, e) EOL MEA with GDL A, (c, f) EOL MEA with GDL B, and (g) particle size histogram of Pt/C in BOL MEA and EOL MEA with GDLs.

GDL A. These FE-TEM analysis results suggest that water management on the GDL under AST conditions has a significant impact on the degradation of the carbon support, which ultimately affects the particle size and distribution of the Pt/C catalyst. These findings suggest a correlation between the characteristics of the GDL and degradation of the carbon support, as well as that between the particle size and distribution of the Pt/C catalyst.

3.4. Driving Force of Water Transport within the GDL. Typically, the addition of PTFE in the GDL facilitates efficient water removal. However, increasing the PTFE content alone does not enhance the water discharge capability. As mentioned in Sections 2.4 and 3.1, although GDL B has a higher PTFE content than GDL A, it possesses a coarse carbon fiber structure, resulting in a poor water discharge capability. This difference contributes to decreased mass transport losses, ultimately affecting fuel cell performance and degradation. The driving force of the liquid water transport is the capillary pressure gradient. The capillary pressure is expressed as follows [19, 33–35]:

$$P_c = \sigma \cos(\theta)\left(C\frac{(1-\varepsilon)}{\varepsilon d_{\mathrm{p}}}\right)J(s), \tag{4}$$

where P_c is the capillary pressure, σ is the surface tension of water, θ is the contact angle, ε is the porosity, d_p is the pore diameter, C is the constant, $J(s)$ is the Leverett J-function, and s is the liquid water saturation level.

$$J(s) = 1.417s - 2.120s^2 + 1.263s^3. \tag{5}$$

Physical properties listed in Table 1 were used to solve Equation (4). Both d_p and ε were obtained from the pore size distribution shown in Figure 3(e). The ε value was determined

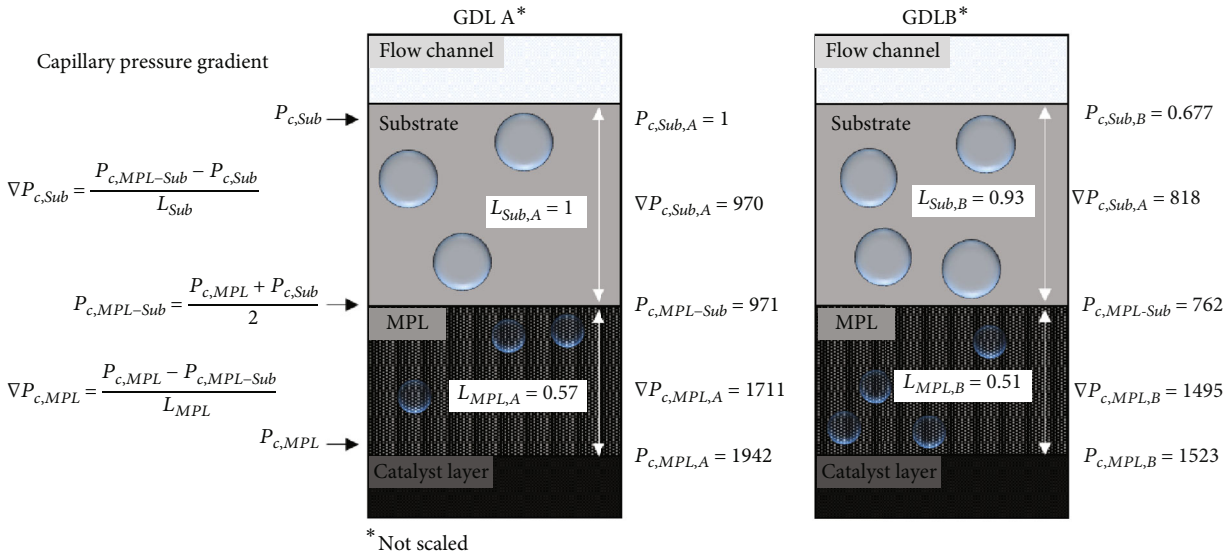

Figure 8: Schematic of capillary pressure gradient through a GDL.

by comparing the relative values of GDL A and GDL B with respect to the substrate and the MPL. Without accounting for the influence of saturation, and comparing solely based on geometric properties, in the case of GDL A, the normalized values of thickness, $1/d_p$, $(1-\varepsilon)/\varepsilon$, and $|\cos(\theta)|$ of substrate are 1, 1, 1, and 1 and MPL are 0.57, 358.11, 4.71, and 1.15, respectively; in the case of GDL B, the corresponding values of the substrate are 0.93, 0.9, 0.71, and 1.05 and MPL are 0.51, 347.74, 3.72, and 1.18, respectively. Figure 8 shows the capillary pressure gradient modeling [35, 36]. In this model, the control volume extends from just below the channel to just above the CL. Therefore, the capillary pressure at the channel and substrate interface is also the capillary pressure in the substrate. Similarly, the capillary pressure at the CL and MPL interface is determined by the capillary pressure in the MPL. The calculated results show that the capillary pressure gradient of GDL A is higher than that of GDL B for both the substrate and the MPL. Hence, water discharge is effective in GDL A. In contrast, water tends to accumulate significantly in GDL B.

4. Conclusions

This study assessed the influence of two commercial GDLs on carbon corrosion in the CL, specifically in relation to water management. The main conclusions can be summarized as follows:

(1) GDL B is thinner and has an overall higher PTFE content than GDL A. However, GDL B has a larger porosity than GDL A because of its coarser substrate structure than the latter. This property is also responsible for a higher gas permeability in GDL B than in GDL A

(2) We observed water behavior using visualization cells and X-ray imaging. The results obtained using the visualization cell indicated that GDL B has a lower water expulsion capability than GDL A. The differences in the water management capability of the two GDLs could be attributed to factors such as pore diameter, porosity, thickness, and contact angle. The combination of properties creates a lower capillary pressure gradient in both the substrate and the MPL, leading to increased water accumulation in GDL B

(3) Both before and after the AST, GDL B exhibited a poorer performance than that shown by GDL A in the same MEA. This is because the retained water could lead to a carbon corrosion reaction in the CL. The increased internal water content hinders the transport of oxygen, eventually leading to mass transport losses. This was also confirmed through a Nyquist plot

(4) The modified DOE-AST method, including constant current operation for water generation reactions, reduces the number of cycles of AST compared to that observed for the original DOE cycle. Hence, it can be concluded that the presence of liquid water accelerates the carbon corrosion and Pt agglomeration in the CL

Data Availability

The data that support the findings of this study are available from the corresponding author upon reasonable request.

Disclosure

This manuscript is an updated version. The earlier version has been presented as a preprint in the following link: https://papers.ssrn.com/sol3/papers.cfm?abstract_id=4570209 [37].

Conflicts of Interest

The authors declare that they have no known competing financial interests or personal relationships that could have appeared to influence the work reported in this paper.

Acknowledgments

This work was supported by the Korea Institute of Energy Technology Evaluation and Planning (KETEP) grant funded by the Korean Government (MOTIE) (grant number 20203010030010).

Supplementary Materials

Figure S1: an overview of the effects of water management in GDLs on carbon corrosion rate in the catalyst layer. Figure S2: SEM images of fresh GDLs measured twice (a) GDL A 1st, (b) GDL A 2nd, (c) GDL B 1st, and (d) GDL B 2nd. Figure S3: TGA curves of GDL A and GDL B in nitrogen for a heating rate of $10^{\circ}C\,min^{-1}$. Figure S4: polarization curves obtained over 3,000 cycles using the modified AST. *(Supplementary Materials)*

References

[1] Y. Duan, H. Liu, W. Zhang, L. Khotseng, Q. Xu, and H. Su, "Materials, components, assembly and performance of flexible polymer electrolyte membrane fuel cell: A review," *Journal of Power Sources*, vol. 555, article 232369, 2023.

[2] D. J. Kim, H. J. Jeong, J. W. Shim et al., "Improving the stability of polymer electrolyte membrane fuel cells via atomic layer-deposited cerium oxide," *International Journal of Energy Research*, vol. 2023, Article ID 5506063, 9 pages, 2023.

[3] Y. Wang, K. S. Chen, J. Mishler, S. C. Cho, and X. C. Adroher, "A review of polymer electrolyte membrane fuel cells: technology, applications, and needs on fundamental research," *Applied Energy*, vol. 88, no. 4, pp. 981–1007, 2011.

[4] J. Zhao, Z. Tu, and S. H. Chan, "Carbon corrosion mechanism and mitigation strategies in a proton exchange membrane fuel cell (PEMFC): a review," *Journal of Power Sources*, vol. 488, article 229434, 2021.

[5] R. T. White, S. H. Eberhardt, Y. Singh et al., "Four-dimensional joint visualization of electrode degradation and liquid water distribution inside operating polymer electrolyte fuel cells," *Scientific Reports*, vol. 9, no. 1, p. 1843, 2019.

[6] Y. Luo, Y. Wu, B. Li et al., "Development and application of fuel cells in the automobile industry," *Journal of Energy Storage*, vol. 42, article 103124, 2021.

[7] F. Sun, D. Su, and Y. Yin, "A streamline dot flow field design for proton exchange membrane fuel cell," *International Journal of Energy Research*, vol. 2023, Article ID 3928657, 12 pages, 2023.

[8] J. Li, H. Liu, W. Zhang et al., "In-situ preparation of low Pt loading multi rhombic-pyramidal Pt–Pd catalyst layer for high-performance proton exchange membrane fuel cells," *Journal of Power Sources*, vol. 556, article 232445, 2023.

[9] U. Pasaogullari and C. Y. Wang, "Two-phase transport and the role of micro-porous layer in polymer electrolyte fuel cells," *Electrochimica Acta*, vol. 49, no. 25, pp. 4359–4369, 2004.

[10] C. J. Tseng and S. K. Lo, "Effects of microstructure characteristics of gas diffusion layer and microporous layer on the performance of PEMFC," *Energy Conversion and Management*, vol. 51, no. 4, pp. 677–684, 2010.

[11] C. A. Reiser, L. Bregoli, T. W. Patterson et al., "A reverse-current decay mechanism for fuel cells," *Electrochemical and Solid-State Letters*, vol. 8, no. 6, pp. A273–A276, 2005.

[12] H. Tang, Z. Qi, M. Ramani, and J. F. Elter, "PEM fuel cell cathode carbon corrosion due to the formation of air/fuel boundary at the anode," *Journal of Power Sources*, vol. 158, no. 2, pp. 1306–1312, 2006.

[13] J. Wu, X. Z. Yuan, J. J. Martin et al., "A review of PEM fuel cell durability: degradation mechanisms and mitigation strategies," *Journal of Power Sources*, vol. 184, no. 1, pp. 104–119, 2008.

[14] P. Saha, K. Khedekar, H. Wang et al., "Correlating the morphological changes to electrochemical performance during carbon corrosion in polymer electrolyte fuel cells," *Journal of Materials Chemistry A*, vol. 10, no. 23, pp. 12551–12562, 2022.

[15] T. Ha, J. Cho, J. Park et al., "Experimental study on carbon corrosion of the gas diffusion layer in polymer electrolyte membrane fuel cells," *International Journal of Hydrogen Energy*, vol. 36, no. 19, pp. 12436–12443, 2011.

[16] S. Yu, X. Li, S. Liu, J. Hao, Z. Shao, and B. Yi, "Study on hydrophobicity loss of the gas diffusion layer in PEMFCs by electrochemical oxidation," *RSC Advances*, vol. 4, no. 8, pp. 3852–3856, 2014.

[17] K. Xu, Q. Di, F. Sun, M. Chen, and H. Wang, "Degradation mechanism analysis of substrate and microporous layer of gas diffusion layer in proton exchange membrane fuel cell," *Fuel*, vol. 358, article 130198, 2024.

[18] X. Zhang, Y. Yang, X. Zhang, and H. Liu, "Identification of performance degradations in catalyst layer and gas diffusion layer in proton exchange membrane fuel cells," *Journal of Power Sources*, vol. 449, article 227580, 2020.

[19] J. Sim, M. Kang, K. Min, E. Lee, and J. Y. Jyoung, "Effects of carbon corrosion on proton exchange membrane fuel cell performance using two durability evaluation methods," *Renewable Energy*, vol. 190, pp. 959–970, 2022.

[20] J. Zhao, Z. Tu, and S. H. Chan, "In-situ measurement of humidity distribution and its effect on the performance of a proton exchange membrane fuel cell," *Energy*, vol. 239, article 122270, 2022.

[21] J. H. Kim, Y. Yeon Jo, E. A. Cho et al., "Effects of cathode inlet relative humidity on PEMFC durability during startup–shutdown cycling," *Journal of the Electrochemical Society*, vol. 157, no. 5, pp. B633–B642, 2010.

[22] J. Kwon, P. Choi, and K. Eom, "A comparison study on the carbon corrosion reaction under saturated and low relative humidity conditions via transmission line model-based electrochemical impedance analysis," *Journal of the Electrochemical Society*, vol. 168, no. 6, article 064515, 2021.

[23] B. Xiao, Z. Huang, Z. Tu, and S. H. Chan, "Water management in a novel proton exchange membrane fuel cell stack with moisture coil cooling," *International Journal of Hydrogen Energy*, vol. 48, no. 28, pp. 10671–10683, 2023.

[24] D. Spernjak, J. Fairweather, R. Mukundan, T. Rockward, and R. L. Borup, "Influence of the microporous layer on carbon corrosion in the catalyst layer of a polymer electrolyte membrane fuel cell," *Journal of Power Sources*, vol. 214, pp. 386–398, 2012.

[25] L. Zuo, Q. Jian, and Y. Yang, "Durability improvement mechanism of proton exchange membrane fuel cell by microporous layer," *International Journal of Energy Research*, vol. 46, no. 13, pp. 18809–18818, 2022.

[26] Fuel cell technical team roadmap, 2017.

[27] Z. Fishman and A. Bazylak, "Heterogeneous through-plane porosity distributions for treated PEMFC GDLs I. PTFE effect," *Journal of The Electrochemical Society*, vol. 158, no. 8, article B841, 2011.

[28] H. Sadeghifar, N. Djilali, and M. Bahrami, "Effect of polytetrafluoroethylene (PTFE) and micro porous layer (MPL) on thermal conductivity of fuel cell gas diffusion layers: modeling and experiments," *Journal of Power Sources*, vol. 248, pp. 632–641, 2014.

[29] G.-G. Park, Y.-J. Sohn, T.-H. Yang, Y.-G. Yoon, W.-Y. Lee, and C.-S. Kim, "Effect of PTFE contents in the gas diffusion media on the performance of PEMFC," *Journal of Power Sources*, vol. 131, no. 1-2, pp. 182–187, 2004.

[30] B. D. Cullity, *Elements of X-Ray Diffraction*, Addison-Wesley Publishing, 1956.

[31] n.d., https://imagej.nih.gov/ij/index.html.

[32] A. Kobayashi, T. Fujii, K. Takeda, K. Tamoto, K. Kakinuma, and M. Uchida, "Effect of Pt loading percentage on carbon blacks with large interior nanopore volume on the performance and durability of polymer electrolyte fuel cells," *ACS Applied Energy Materials*, vol. 5, no. 1, pp. 316–329, 2022.

[33] J. Cho, J. Park, H. Oh, K. Min, E. Lee, and J. Y. Jyoung, "Analysis of the transient response and durability characteristics of a proton exchange membrane fuel cell with different micro-porous layer penetration thicknesses," *Applied Energy*, vol. 111, pp. 300–309, 2013.

[34] H. Oh, J. Park, K. Min, E. Lee, and J.-Y. Jyoung, "Effects of pore size gradient in the substrate of a gas diffusion layer on the performance of a proton exchange membrane fuel cell," *Applied Energy*, vol. 149, pp. 186–193, 2015.

[35] J. Cho, H. Oh, J. Park, K. Min, E. Lee, and J. Y. Jyoung, "Effect of the micro porous layer design on the dynamic performance of a proton exchange membrane fuel cell," *International Journal of Hydrogen Energy*, vol. 39, no. 1, pp. 459–468, 2014.

[36] J. Sim, M. Kang, and K. Min, "Effects of basic gas diffusion layer components on PEMFC performance with capillary pressure gradient," *International Journal of Hydrogen Energy*, vol. 46, no. 54, pp. 27731–27748, 2021.

[37] S. Lee, C. Kim, E. Lee et al., "Effects of gas-diffusion layers and water management on the carbon corrosion of a catalyst layer in proton-exchange membrane fuel cells," 2023, https://ssrn.com/abstract=4570209.